Title	A large strain finite volume method for orthotropic bodies with general material orientations
Authors(s)	Cardiff, Philip, Karac, Aleksandar, Ivankovic, Alojz
Publication date	2014-01
Publication information	Cardiff, Philip, Aleksandar Karac, and Alojz Ivankovic. “A Large Strain Finite Volume Method for Orthotropic Bodies with General Material Orientations.” Elsevier, January 2014. https://doi.org/10.1016/j.cma.2013.09.008.
Publisher	Elsevier
Item record/more information	http://hdl.handle.net/10197/5922
Publisher's statement	This is the author's version of a work that was accepted for publication in Computer Methods in Applied Mechanics and Engineering. Changes resulting from the publishing process, such as peer review, editing, corrections, structural formatting, and other quality control mechanisms may not be reflected in this document. Changes may have been made to this work since it was submitted for publication. A definitive version was subsequently published in Computer Methods in Applied Mechanics and Engineering (268, , (2014)) DOI: http://dx.doi/org/10.1016/j.cma.2013.09.008
Publisher's version (DOI)	10.1016/j.cma.2013.09.008

A Large Strain Finite Volume Method for Orthotropic Bodies with General Material Orientations

P.Cardiff[a,*], A.Karač[b], A.Ivanković[a]

[a] *School of Mechanical and Materials Engineering, University College Dublin, Belfield, D4, Dublin, Ireland*
[b] *Faculty of Mechanical Engineering, University of Zenica, Fakultetska 1, 72000 Zenica, Bosnia and Herzegovina*

Abstract

This paper describes a finite volume method for orthotropic bodies with general principal material directions undergoing large strains and large rotations. The governing and constitutive relations are presented and the employed updated Lagrangian mathematical model is outlined. In order to maintain equivalence with large strain total Lagrangian methods, the constitutive stiffness tensor is updated transforming the principal material directions to the deformed configuration. Discretisation is performed using the cell-centred finite volume method for unstructured convex polyhedral meshes. The current methodology is successfully verified by numerically examining two separate test cases: a circular hole in an orthotropic plate subjected to a traction and a rotating orthotropic plate containing a hole subjected to a pressure. The numerical predictions have been shown to agree closely with the available analytical solutions. In addition, a 3-D composite component is examined to demonstrate the capabilities of the developed methodology in terms of a

---

[*] Corresponding author. *Tel.*: +353 1 716 1880
Email address: `philip.cardiff@ucd.ie` (P.Cardiff)

Preprint submitted to Computer Methods in Applied Mechanics and Engineering August 28, 2013

variable material orientation and parallel processing.

Keywords: orthotropic elasticity; finite volume method; large strain; updated Lagrangian; OpenFOAM

---

1. Introduction

Composite materials are finding greater importance in many engineering applications such as aerospace and renewable energy due to their high strength-to-weight ratio and superior mechanical and thermal properties. Accurate calculation of the mechanics of these orthotropic systems is of considerable importance in the design of such structures.

The finite element (FE) and finite volume (FV) methods are commonly employed in computational solid mechanics (CSM) and computational fluid dynamics (CFD), where the FE method is traditionally associated with CSM and the FV method associated with CFD. However, the usage of FV analysis in CSM is becoming increasingly popular due to the attractively simple yet strongly conservative nature of the method. At present, the FV method has been applied to a large range of stress analysis problems in linear-elasticity [1, 2, 3, 4, 5, 6, 7, 8], thermo-elastoplasticity [9], thermo-viscoelasticity [10], incompressible elasticity [11, 12], contact mechanics [14, 15, 16, 17, 18], fracture mechanics [19, 20, 21, 22, 23, 24, 25, 26, 27, 28, 29, 30, 31, 32] and fluid-structure interactions [27, 33, 34, 35].

Even though a wide variety of solid mechanics problems have been analysed using the FV method, orthotropic bodies with general material directions experiencing large strains and rotations have yet to be analysed. Fainberg et al. [36] developed a 2-D orthotropic solver employing the FV method for coupled thermo-elastic analyses within a cylindrical reference frame. Demirdžić et al. [37] developed a 3-D FV procedure for the analysis of orthotropic bodes undergoing small strains, where the principal material directions align with the global Cartesian axes. The current research adopts similar approaches to Fainberg et al. [36] and Demirdžić et al. [37] and extends their methods to allow for large strains and large rotations. Additionally, the principal material directions are general and may be aligned in any direction and spatially varying, allowing more complex structures such as aircraft wings, turbine blades and other composite components to be examined. Furthermore, the currently adopted large strain FV approach would allow consistent and efficient fluid-structure interaction analyses to be performed on orthotropic structures.

This paper describes the development and verification of a large strain FV procedure for the analysis of orthotropic bodies with general principal material directions. The procedure is implemented as a custom application in open-source software OpenFOAM (version 1.6-ext) [38, 39].

2. Mathematical Model

2.1. Governing Equation

For an arbitrary body of volume Ω, bounded by surface Γ with unit normal $\boldsymbol{n}$, the conservation of linear momentum in integral form is given by:

$$\overbrace{\frac{\partial}{\partial t}\int_{\Omega} \rho\, \boldsymbol{v}\, d\Omega}^{\text{Inertia}} = \overbrace{\oint_{\Gamma} \boldsymbol{n} \cdot \boldsymbol{\sigma}\, d\Gamma}^{\text{Surface Forces}} + \overbrace{\int_{\Omega} \rho\, \boldsymbol{b}\, d\Omega}^{\text{Body Forces}} \tag{1}$$

where $\boldsymbol{v}$ is the velocity vector, $\boldsymbol{\sigma}$ is the Cauchy stress tensor, ρ is the density, and $\boldsymbol{b}$ is the body force per unit mass. The linear momentum equality, a generalisation of Newton's second law of motion, states that the rate of change of the total linear momentum of a body is equal to the sum of all the forces acting on the body. As the current study adopts a Lagrangian approach, the convection term is zero *i.e.* there is no mass flow across the surface of the volume of interest.

2.2. Constitutive Relation

For elastic materials, the relationship between stress and strain is governed by the generalised Hooke's theory of elasticity in incremental form:

$$\delta \boldsymbol{S} = \boldsymbol{C} : \delta \boldsymbol{E} \tag{2}$$

where $\delta \boldsymbol{S}$ is the increment of second Piola-Kirchhoff stress tensor, $\delta \boldsymbol{E}$ is the increment of Green strain tensor, and $\boldsymbol{C}$ is the fourth-order constitutive tensor of elastic constants. The operator : signifies a double dot product. The increment of Green strain is given by:

$$\delta \boldsymbol{E} = \frac{1}{2}\left[\nabla \delta \boldsymbol{u} + \nabla \delta \boldsymbol{u}^T + \nabla \delta \boldsymbol{u} \cdot \nabla \boldsymbol{u}^T + \nabla \boldsymbol{u} \cdot \nabla \delta \boldsymbol{u}^T + \nabla \delta \boldsymbol{u} \cdot \nabla \delta \boldsymbol{u}^T\right] \tag{3}$$

where $\delta \boldsymbol{u}$ is the increment of displacement and ∇ signifies the so called *Hamilton* operator, synonymous with the *del* or *nabla* operator.

For an isotropic linear elastic material, the 81 components of the elastic stiffness tensor, $\boldsymbol{C}$, reduce to two independent material parameters. In contrast, for an orthotropic linear elastic material, the 81 components reduce to nine independent material parameters. The generalised Hooke's law (Equation 2) for an orthotropic linear elastic material may be rewritten in the Voight 6×6 matrix notation [40, 37]:

$$\begin{pmatrix} \delta\boldsymbol{S}_{xx} \\ \delta\boldsymbol{S}_{yy} \\ \delta\boldsymbol{S}_{zz} \\ \delta\boldsymbol{S}_{xy} \\ \delta\boldsymbol{S}_{yz} \\ \delta\boldsymbol{S}_{zx} \end{pmatrix} = \begin{pmatrix} A_{11} & A_{12} & A_{31} & 0 & 0 & 0 \\ A_{12} & A_{22} & A_{23} & 0 & 0 & 0 \\ A_{31} & A_{23} & A_{33} & 0 & 0 & 0 \\ 0 & 0 & 0 & A_{44} & 0 & 0 \\ 0 & 0 & 0 & 0 & A_{55} & 0 \\ 0 & 0 & 0 & 0 & 0 & A_{66} \end{pmatrix} \begin{pmatrix} \delta\boldsymbol{E}_{xx} \\ \delta\boldsymbol{E}_{yy} \\ \delta\boldsymbol{E}_{zz} \\ \delta\boldsymbol{E}_{xy} \\ \delta\boldsymbol{E}_{yz} \\ \delta\boldsymbol{E}_{zx} \end{pmatrix} \tag{4}$$

where the stiffness coefficients, A_{ij}, are given in terms of Young's moduli, E_i, Poisson's ratio, ν_{ij}, and shear moduli, G_{ij}, by:

$$\begin{aligned} &A_{11} = \frac{1 - \nu_{23}\nu_{32}}{A_0 E_2 E_3},\ A_{22} = \frac{1 - \nu_{13}\nu_{31}}{A_0 E_1 E_3},\ A_{33} = \frac{1 - \nu_{21}\nu_{12}}{A_0 E_2 E_1}, \\ &A_{12} = \frac{\nu_{12} + \nu_{32}\nu_{13}}{A_0 E_1 E_3},\ A_{23} = \frac{\nu_{23} + \nu_{21}\nu_{13}}{A_0 E_1 E_2},\ A_{31} = \frac{\nu_{31} + \nu_{21}\nu_{32}}{A_0 E_2 E_3}, \\ &A_{44} = 2G_{12},\ A_{55} = 2G_{23},\ A_{66} = 2G_{31}, \\ &A_0 = \frac{1 - \nu_{12}\nu_{21} - \nu_{23}\nu_{32} - \nu_{13}\nu_{31} - 2\nu_{21}\nu_{32}\nu_{13}}{E_1 E_2 E_3}. \end{aligned} \tag{5}$$

The three Young's moduli E_1, E_2 and E_3 correspond to the stiffness in the global x, y and z directions, respectively. The Poisson's ratio ν_{ij} corresponds to the transverse strain in the j direction due to a strain in the i direction. In general, $\nu_{ij} \neq \nu_{ji}$, and they are connected by the relation $\frac{\nu_{ij}}{E_i} = \frac{\nu_{ji}}{E_j}$. The shear modulus in the ij plane is G_{ij} and obeys the relation $G_{ij} = G_{ji}$.

As the material properties are commonly known in their local and not the global coordinate system, a field of local constitutive stiffness tensors, $\boldsymbol{C}_{\text{local}}$, is constructed at the beginning of the simulation using the user specified properties. Subsequently, by employing the user specified initial principal material directions, the local constitutive tensor field is rotated to the global coordinate system:

$$\boldsymbol{C} = \boldsymbol{A}^T \cdot \boldsymbol{C}_{\text{local}} \cdot \boldsymbol{A} \tag{6}$$

where tensor $\boldsymbol{A}$ is given by:

$$\begin{pmatrix}
L_{xx}^2 & L_{xy}^2 & L_{xz}^2 & \sqrt{2}L_{xx}L_{xy} & \sqrt{2}L_{xy}L_{xz} & \sqrt{2}L_{xz}L_{xx} \\
L_{yx}^2 & L_{yy}^2 & L_{yz}^2 & \sqrt{2}L_{yx}L_{yy} & \sqrt{2}L_{yy}L_{yz} & \sqrt{2}L_{yz}L_{yx} \\
L_{zx}^2 & L_{zy}^2 & L_{zz}^2 & \sqrt{2}L_{zx}L_{zy} & \sqrt{2}L_{zy}L_{zz} & \sqrt{2}L_{zz}L_{zx} \\
\sqrt{2}L_{xx}L_{yx} & \sqrt{2}L_{xy}L_{yy} & \sqrt{2}L_{xz}L_{yz} & \begin{matrix}(L_{xy}L_{yx} \\ +L_{xx}L_{yy})\end{matrix} & \begin{matrix}(L_{xz}L_{yy} \\ +L_{xy}L_{yz})\end{matrix} & \begin{matrix}(L_{xx}L_{yz} \\ +L_{xz}L_{yx})\end{matrix} \\
\sqrt{2}L_{yx}L_{zx} & \sqrt{2}L_{yy}L_{zy} & \sqrt{2}L_{yz}L_{zz} & \begin{matrix}(L_{yy}L_{zx} \\ +L_{yx}L_{zy})\end{matrix} & \begin{matrix}(L_{yz}L_{zy} \\ +L_{yy}L_{zz})\end{matrix} & \begin{matrix}(L_{yx}L_{zz} \\ +L_{yz}L_{zx})\end{matrix} \\
\sqrt{2}L_{zx}L_{xx} & \sqrt{2}L_{zy}L_{xy} & \sqrt{2}L_{zz}L_{xz} & \begin{matrix}(L_{zy}L_{xx} \\ +L_{zx}L_{xy})\end{matrix} & \begin{matrix}(L_{zz}L_{xy} \\ +L_{zy}L_{xz})\end{matrix} & \begin{matrix}(L_{zx}L_{xz} \\ +L_{zz}L_{xx})\end{matrix}
\end{pmatrix} \tag{7}$$

and the components of the second order tensor $\boldsymbol{L}$ are given by $\boldsymbol{x}_i \cdot \boldsymbol{y}_j$:

$$\boldsymbol{L} = \begin{pmatrix}
\boldsymbol{x}_1 \cdot \boldsymbol{y}_1 & \boldsymbol{x}_1 \cdot \boldsymbol{y}_2 & \boldsymbol{x}_1 \cdot \boldsymbol{y}_3 \\
\boldsymbol{x}_2 \cdot \boldsymbol{y}_1 & \boldsymbol{x}_2 \cdot \boldsymbol{y}_2 & \boldsymbol{x}_2 \cdot \boldsymbol{y}_3 \\
\boldsymbol{x}_3 \cdot \boldsymbol{y}_1 & \boldsymbol{x}_3 \cdot \boldsymbol{y}_2 & \boldsymbol{x}_3 \cdot \boldsymbol{y}_3
\end{pmatrix} \tag{8}$$

where $\boldsymbol{x}_1$, $\boldsymbol{x}_2$ and $\boldsymbol{x}_3$ are the global coordinate base unit vectors and $\boldsymbol{y}_1$, $\boldsymbol{y}_2$ and $\boldsymbol{y}_3$ are the local coordinate base unit vectors supplied by the user.

It should be noted that although the current method is developed employing an orthotropic version of the classical Kirchhoff–St. Venant elasticity model, it may be extended in a straight-forward manner to allow more complex constitutive behaviours, such as quasi-incompressibility [11, 12, 13].

2.3. Updated Lagrangian Mathematical Model

To derive the mathematical model for the updated Lagrangian approach, the conservation of linear momentum (Equation 1) may be written in terms of the second Piola-Kirchhoff stress tensor:

$$\frac{\partial}{\partial t}\int_{\Omega_o} \rho\, \boldsymbol{v}\, d\Omega_o = \oint_{\Gamma_o} \boldsymbol{n}_o \cdot (\boldsymbol{S}_o \cdot \boldsymbol{F}_o)\, d\Gamma_o + \int_{\Omega_o} \rho\, \boldsymbol{b}\, d\Omega_o \tag{9}$$

where quantities appended by subscript o are referred to the original undeformed configuration, the deformation gradient $\boldsymbol{F} = \boldsymbol{I} + \nabla \boldsymbol{u}$, and $\boldsymbol{I}$ is the second order identity tensor. The relation may be written in the incremental form by employing the finite difference method:

$$\frac{\partial}{\partial t}\int_{\Omega_o} \rho\, \delta\boldsymbol{v}\, d\Omega_o = \oint_{\Gamma_o} \boldsymbol{n}_o \cdot (\delta\boldsymbol{S}_o \cdot \boldsymbol{F}_o + \boldsymbol{S}_o \cdot \delta\boldsymbol{F}_o + \delta\boldsymbol{S}_o \cdot \delta\boldsymbol{F}_o)\, d\Gamma_o + \int_{\Omega_o} \rho\, \delta\boldsymbol{b}\, d\Omega_o \tag{10}$$

By noting that $\nabla \boldsymbol{u} = 0$ when the updated Lagrangian approach is employed, Equation 10 may be simplified:

$$\frac{\partial}{\partial t}\int_{\Omega_u} \rho\, \delta\boldsymbol{v}\, d\Omega_u = \oint_{\Gamma_u} \boldsymbol{n}_u \cdot (\delta\boldsymbol{S} + \boldsymbol{S} \cdot \delta\boldsymbol{F} + \delta\boldsymbol{S} \cdot \delta\boldsymbol{F})\, d\Gamma_u + \int_{\Omega_u} \rho\, \delta\boldsymbol{b}\, d\Omega_u \tag{11}$$

The presented updated Lagrangian mathematical model ensures that the increment of force for each time increment is in equilibrium. However, as only the increment of force is considered and not that total force equilibrium, this approach may be susceptible to the build-up of numerical errors. Accordingly, Equation 11 may be modified to ensure that the total forces are in equilibrium by including any imbalance from the previous increment:

$$\begin{aligned} \frac{\partial}{\partial t}\int_{\Omega_u} \rho\, \frac{\partial(\boldsymbol{u} + \delta\boldsymbol{u})}{\partial t}\, d\Omega_u \quad &= \quad \oint_{\Gamma_u} \boldsymbol{n}_u \cdot (\delta\boldsymbol{S}_u + \boldsymbol{S}_u + \boldsymbol{S}_u \cdot \delta\boldsymbol{F}_u + \delta\boldsymbol{S}_u \cdot \delta\boldsymbol{F}_u)\, d\Gamma_u \\ &\quad + \int_{\Omega_u} \rho\, (\boldsymbol{b} + \delta\boldsymbol{b})\, d\Omega_u \end{aligned} \tag{12}$$

Due to the current modifications, the current increment of force can compensate for any slight imbalance from previous steps thus ensuring equilibrium of the total forces. The effect of this modification is highlighted in the test case section.

Substituting the constitutive law, Equation 2, into the updated Lagrangian momentum equation (Equation 11) yields the linear momentum equation for the updated Lagrangian method:

$$\begin{aligned}\frac{\partial}{\partial t}\int_{\Omega_u}\rho\frac{\partial(\boldsymbol{u}+\delta\boldsymbol{u})}{\partial t}\,d\Omega_u \;&=\; \oint_{\Gamma_u}\boldsymbol{n}_u\cdot\left(\boldsymbol{C}_u:\delta\boldsymbol{E}_u\right)\,d\Gamma_u\\ &+\oint_{\Gamma_u}\boldsymbol{n}_u\cdot\left[\left(\boldsymbol{S}_u+\delta\boldsymbol{S}_u\right)\cdot\nabla\delta\boldsymbol{u}\right]\,d\Gamma_u\\ &+\oint_{\Gamma_u}\boldsymbol{n}_u\cdot\boldsymbol{S}_u\,d\Gamma_u\\ &+\int_{\Omega_u}\rho\,\left(\boldsymbol{b}+\delta\boldsymbol{b}\right)\,d\Omega_u \end{aligned} \tag{13}$$

where $\delta\boldsymbol{F}_u=\nabla\delta\boldsymbol{u}$, and the increment of Green strain (Equation 3) reduces to:

$$\delta\boldsymbol{E}_u=\frac{1}{2}\left(\nabla\delta\boldsymbol{u}+\nabla\delta\boldsymbol{u}^T+\nabla\delta\boldsymbol{u}\cdot\nabla\delta\boldsymbol{u}^T\right) \tag{14}$$

To allow the system (Equation 13) to be solved using a segregated solution procedure, the first term on the right hand side of Equation 13 is decomposed into an implicit and an explicit component treated using a lagged correction approach, leading to

$$\begin{aligned}\frac{\partial}{\partial t}\int_{\Omega_u}\rho_u\frac{\partial(\boldsymbol{u}+\delta\boldsymbol{u})}{\partial t}\,d\Omega_u \;&=\; \overbrace{\oint_{\Gamma_u}\boldsymbol{n}_u\cdot\left(\boldsymbol{K}\cdot\nabla\delta\boldsymbol{u}\right)\,d\Gamma_u}^{\text{Implicit Component}}\\ &+\overbrace{\oint_{\Gamma_u}\boldsymbol{n}_u\cdot\boldsymbol{Q}_\Gamma\,d\Gamma_u}^{\text{Explicit Term}}+\int_{\Omega_u}\rho_u\left[\boldsymbol{b}+\delta\boldsymbol{b}\right]d\Omega_u \end{aligned} \tag{15}$$

where the explicit diffusion term, $\boldsymbol{Q}_\Gamma$, is given by:

$$\boldsymbol{Q}_\Gamma \;=\; \boldsymbol{C}_u:\delta\boldsymbol{E}_u-\boldsymbol{K}\cdot\nabla\delta\boldsymbol{u}+\left[\boldsymbol{S}_u+\delta\boldsymbol{S}_u\right]\cdot\nabla\delta\boldsymbol{u}+\boldsymbol{S}_u \tag{16}$$

and the tensor $\boldsymbol{K}$ is given by:

$$\boldsymbol{K} = \begin{pmatrix} A_{11} & 0 & 0 \\ 0 & A_{22} & 0 \\ 0 & 0 & A_{33} \end{pmatrix} \tag{17}$$

At the end of each time increment, the accumulated total stress, strain and displacement fields are found by addition of the value from the previous time instant t and increment during dt:

$$\begin{aligned} \boldsymbol{\phi}^{[t+dt]} &= \boldsymbol{\phi}^{[t]} + \int_t^{t+dt} \dot{\boldsymbol{\phi}}\, dt \\ &\approx \boldsymbol{\phi}^{[t]} + \delta\boldsymbol{\phi}^{[t+dt]} \end{aligned} \tag{18}$$

where $\boldsymbol{\phi}$ represents $\boldsymbol{S}$, $\boldsymbol{E}$ and $\boldsymbol{u}$. The density is found by:

$$\rho^{[t+dt]} = \frac{1}{J^{[t+dt]}}\, \rho^{[t]} \tag{19}$$

where the Jacobian, J, is the determinant of $\boldsymbol{F}$.

Before proceeding to the next time increment, the configuration is updated such that the current configuration becomes the reference configuration. The accumulated stress and strain tensors are updated by the transformations [41, 42, 22, 43]:

$$\boldsymbol{E}_u = \boldsymbol{F}^{-1} \cdot \boldsymbol{E} \cdot (\boldsymbol{F}^{-1})^T \tag{20}$$

$$\boldsymbol{S}_u = \frac{1}{J}\, \boldsymbol{F}^T \cdot \boldsymbol{S} \cdot \boldsymbol{F} \tag{21}$$

Additionally, for equivalence with large strain total Lagrangian approaches, the constitutive stiffness tensor must be updated [41, 42, 22]:

$$\boldsymbol{C}_u = \boldsymbol{A}^T \cdot \boldsymbol{C} \cdot \boldsymbol{A} \tag{22}$$

where tensor $\boldsymbol{A}$ is given by Equation 7 except the transpose of the deformation gradient $\boldsymbol{F}^T$ is employed instead of tensor $\boldsymbol{L}$.

3. Numerical Method

The mathematical models of the governing equations presented in the preceding section are now discretised using the cell-centred finite volume method. It is important to note that the discretisation process provides a discrete approximate version of the previously presented exact integral relations. The discretisation procedure is separated into two distinct parts: discretisation of the solution domain and discretisation of the governing equations.

3.1. Solution Domain

Discretisation of the solution domain comprises the discretisation of time and the discretisation of space. The total specified simulation time is divided into a finite number of time increments, δt, and the discretised linear momentum mathematical model is solved in a time-marching manner. The solution domain space is split into a finite number of convex polyhedral cells bounded by polygonal faces. The cells do not overlap and fill the space completely. A typical control volume is shown in Figure 1, with the computational node P located at the cell centroid, the cell volume is Ω_P, N is the centroid of a neighbouring control volume, face f has face area vector $\boldsymbol{\Gamma}_f$, vector $\boldsymbol{d}_f$ joins P to N and $\boldsymbol{r}$ is the positional vector of P.

3.2. Equations

As can be seen in Equation 15, the surface diffusion term is divided into an implicit component and an explicit component. The explicit component, $\boldsymbol{Q}_\Gamma$, contains cross-equation coupling and nonlinear terms and is treated explicitly using an iterative lagged corrected approach to allow use of a segregated solution procedure. The equations of mathematical model are solved independently for each displacement increment (Cartesian) component. In each time increment, outer iterations are performed over the system until the explicit components have converged.

Temporal Term

For time m, the time derivative of $\delta\boldsymbol{u}$ at cell centre P is calculated using a first order fully implicit Euler time scheme:

$$\left(\frac{\partial(\delta\boldsymbol{u}_P)}{\partial t}\right)^{[m]} \approx \frac{\delta\boldsymbol{u}_P^{[m]} - \delta\boldsymbol{u}_P^{[m-1]}}{\delta t^{[m]}} \tag{23}$$

where the current time increment is indicated by subscript $[m]$, while the previous time increment is indicated by subscript $[m-1]$.

The rate of change temporal term for control volume P is approximated as:

$$\frac{\partial}{\partial t}\int_{\Omega_u}\rho\frac{\partial(\delta\boldsymbol{u})}{\partial t}\,d\Omega_u \;\approx\; \frac{1}{\delta t^{[m]}}\left[(\rho\frac{\delta(\delta\boldsymbol{u})}{\delta t}\Omega)_P^{[m]} - (\rho\frac{\delta(\delta\boldsymbol{u})}{\delta t}\Omega)_P^{[m-1]}\right] \tag{24}$$

The final discretised temporal term in the linear momentum equation for control volume P, representing the inertia of body, is found by substituting Equation 23 into Equation 24:

$$\begin{aligned}\frac{\partial}{\partial t}\int_{\Omega_u}\rho\frac{\partial(\delta\boldsymbol{u})}{\partial t}\,d\Omega_u \quad &\approx \quad \frac{1}{\delta t^{[m]}}\Bigg[(\rho\Omega)_P^{[m]}\left(\frac{\delta\boldsymbol{u}_P^{[m]} - \delta\boldsymbol{u}_P^{[m-1]}}{\delta t^{[m]}}\right)\\ &\qquad -(\rho\Omega)_P^{[m-1]}\left(\frac{\delta\boldsymbol{u}_P^{[m-1]} - \delta\boldsymbol{u}_P^{[m-2]}}{\delta t^{[m-1]}}\right)\Bigg]\end{aligned} \tag{25}$$

The component of the temporal term containing $\boldsymbol{u}$ is discretised in a similar fashion to Equation 25 but the term is calculated in an entirely explicit manner.

Diffusion Term

The implicit surface diffusion term (Laplacian term) for a cell P may be discretised by assuming a linear variation of $\delta\boldsymbol{u}$ across face f. The orthogonal component of the discrete face normal gradients are treated in an implicit manner, while non-orthogonal components are treated explicitly using a deferred correction approach [2, 16]:

$$\begin{aligned}
\oint_{\Gamma} \boldsymbol{n}_u \cdot (\boldsymbol{K} \cdot \nabla\delta\boldsymbol{u})\ d\Gamma_u &= \sum_{f=1}^{F} \int_{\Gamma_f} \boldsymbol{n}_f \cdot \left[\boldsymbol{K}_{u_f} \cdot (\nabla\delta\boldsymbol{u})_f\right]\ d\Gamma_f \\
&\approx \overbrace{\sum_{f=1}^{F} \left[\boldsymbol{n}_f \cdot (\boldsymbol{n}_f \cdot \boldsymbol{K}_{u_f})\right]\ |\boldsymbol{\Delta}_f| \frac{\delta\boldsymbol{u}_N - \delta\boldsymbol{u}_P}{|\boldsymbol{d}_f|} |\boldsymbol{\Gamma}_f|}^{\text{Implicit}} \\
&\quad + \sum_{f=1}^{F} \left[(\boldsymbol{I} - \boldsymbol{n}_f\boldsymbol{n}_f) \cdot (\boldsymbol{n}_f \cdot \boldsymbol{K}_{u_f})\right] \cdot (\nabla\delta\boldsymbol{u})_f\, |\boldsymbol{\Gamma}_f| \\
&\quad + \sum_{f=1}^{F} \left[\boldsymbol{n}_f \cdot (\boldsymbol{n}_f \cdot \boldsymbol{K}_{u_f})\right]\ \boldsymbol{k}_f \cdot (\nabla\delta\boldsymbol{u})_f\, |\boldsymbol{\Gamma}_f| \qquad (26)
\end{aligned}$$

where F is the number of internal faces in cell P, $\boldsymbol{\Delta}_f = \frac{\boldsymbol{d}_f}{\boldsymbol{d}_f \cdot \boldsymbol{n}_f}$, $\boldsymbol{k}_f = \boldsymbol{n}_f - \boldsymbol{\Delta}_f$, and $\boldsymbol{n}_f$ is the unit normal of the face. The explicit gradient terms are calculated using the least squares approach[1] [2, 16].

---

[1] The OpenFOAM `extendedLeastSquares` gradient scheme is employed as it assumes non-orthogonal boundary cells, unlike the `leastSquares` gradient scheme.

Surface Source Term

The explicit diffusion surface source term is discretised by assuming a linear variation of the source across the face:

$$\begin{aligned}\oint_{\Gamma_u} \boldsymbol{n}_u \cdot \boldsymbol{Q}_\Gamma \; d\Gamma_u &= \sum_{f=1}^{F} \int_{\Gamma_f} \boldsymbol{n}_f \cdot \boldsymbol{Q}_\Gamma \; d\Gamma_f \\ &\approx \sum_{f=1}^{F} \boldsymbol{\Gamma}_f \cdot \boldsymbol{Q}_\Gamma \end{aligned} \tag{27}$$

The discretised surface source term, $\boldsymbol{\Gamma}_f \cdot \boldsymbol{Q}_\Gamma$, is given by Equation 28, where subscript f refers to quantities linearly interpolated to face f. The surface source term contains inter-equation coupling terms and nonlinear terms.

$$\begin{aligned}\boldsymbol{\Gamma}_f \cdot \boldsymbol{Q}_\Gamma &= \boldsymbol{\Gamma}_f \cdot \left(\boldsymbol{C}_u : \delta \boldsymbol{E}_u\right)_f - \boldsymbol{\Gamma}_f \cdot \left(\boldsymbol{K} \cdot \nabla \delta \boldsymbol{u}\right)_f \\ &\quad + \boldsymbol{\Gamma}_f \cdot \left[\left(\boldsymbol{S}_u + \delta \boldsymbol{S}_u\right) \cdot \nabla \delta \boldsymbol{u}\right]_f + \boldsymbol{\Gamma}_f \cdot \boldsymbol{S}_u \end{aligned} \tag{28}$$

Volume Source Term

In a similar fashion, by assuming a linear variation, the body force source term from the volume integral is discretised as:

$$\int_\Omega \rho \, \left(\boldsymbol{b} + \delta \boldsymbol{b}\right) \; d\Omega \; \approx \; \rho \, \left(\boldsymbol{b} + \delta \boldsymbol{b}\right) \; \Omega_P \tag{29}$$

Boundary Conditions

The discretisation of the linear momentum equation has been described for internal mesh faces, while boundary faces require special attention to incorporate them into the mathematical models. This section outlines the implementation of the displacement and traction boundary conditions, where boundary non-orthogonal correction is included as it has been shown to have a large effect in FV solid mechanics [44].

Displacement. The displacement boundary condition, a Dirichlet condition, may be constant in time or time-varying and fixes the value of $\delta\boldsymbol{u}$ at the centre of a boundary face. The specified boundary face value, $\delta\boldsymbol{u}_b$, is substituted into the calculation of the surface flux in Equation 26. Assuming a linear variation across the face, the resulting discretised diffusion term for boundary face b becomes:

$$\begin{aligned}\int_{\Gamma_b} \boldsymbol{n}_b \cdot \left(\boldsymbol{K}_{u_b} \cdot \nabla\delta\boldsymbol{u}_b\right)\, d\Gamma_b \quad \approx \quad & \left[\boldsymbol{n}_b \cdot (\boldsymbol{n}_b \cdot \boldsymbol{K}_{u_b})\right]\, |\boldsymbol{\Delta}_b| \frac{\delta\boldsymbol{u}_b - \delta\boldsymbol{u}_P}{|\boldsymbol{d}_b|} |\boldsymbol{\Gamma}_b| \\ & + \left[(\boldsymbol{I} - \boldsymbol{n}_b\boldsymbol{n}_b) \cdot (\boldsymbol{n}_b \cdot \boldsymbol{K}_{u_b})\right] \cdot (\nabla\delta\boldsymbol{u})_b |\boldsymbol{\Gamma}_b| \\ & + \left[\boldsymbol{n}_b \cdot (\boldsymbol{n}_b \cdot \boldsymbol{K}_{u_b})\right] \boldsymbol{k}_b \cdot (\nabla\delta\boldsymbol{u})_b |\boldsymbol{\Gamma}_b|\end{aligned} \tag{30}$$

where $\boldsymbol{\Delta}_b = \frac{\boldsymbol{d}_b}{\boldsymbol{d}_b \cdot \boldsymbol{n}_b}$, and $\boldsymbol{k}_b = \boldsymbol{n}_b - \boldsymbol{\Delta}_b$.

Traction. The traction boundary condition, constant in time or time-varying, is implemented as a Neumann condition where the normal gradient, $\boldsymbol{g}_b$, of the displacement increment is specified on the boundary face. The specified normal boundary gradient $\boldsymbol{g}_b$ may be directly substituted into the discretised diffusion term, Equation 26:

$$\begin{aligned}\int_{\Gamma_b} \boldsymbol{n}_b \cdot \left(\boldsymbol{K}_{u_b} \cdot \nabla\delta\boldsymbol{u}_b\right)\, d\Gamma_b \quad \approx \quad & \left[\boldsymbol{n}_b \cdot (\boldsymbol{n}_b \cdot \boldsymbol{K}_{u_b})\right]\, \boldsymbol{g}_b |\boldsymbol{\Gamma}_b| \\ & + \left[(\boldsymbol{I} - \boldsymbol{n}_b\boldsymbol{n}_b) \cdot (\boldsymbol{n}_b \cdot \boldsymbol{K}_{u_b})\right] \cdot (\nabla\delta\boldsymbol{u})_b |\boldsymbol{\Gamma}_b| \\ & + \left[\boldsymbol{n}_b \cdot (\boldsymbol{n}_b \cdot \boldsymbol{K}_{u_b})\right] \boldsymbol{k}_b \cdot (\nabla\delta\boldsymbol{u})_b |\boldsymbol{\Gamma}_b|\end{aligned} \tag{31}$$

In order to calculate the normal boundary gradient corresponding to the specified traction, the expression for the boundary traction, $\delta\boldsymbol{T}_b^u$, is employed:

$$\delta\boldsymbol{T}_b^u = \boldsymbol{n}_b \cdot \delta\boldsymbol{\sigma}_b = \overbrace{\boldsymbol{n}_b \cdot [\boldsymbol{K}_b \cdot (\nabla\delta\boldsymbol{u})_b]}^{\text{Implicit Term}} + \overbrace{\boldsymbol{n}_b \cdot [\boldsymbol{C}_b : \delta\boldsymbol{E}_b - \boldsymbol{K}_b \cdot (\nabla\delta\boldsymbol{u})_b]}^{\text{Explicit Term}} \tag{32}$$

Making use of matrix algebraic operations, the expression for the boundary traction, Equation 32, is rearranged to give the implicit boundary normal gradient, $\boldsymbol{g}_b$:

$$\begin{aligned} \boldsymbol{g}_b &= \boldsymbol{n}_b \cdot (\nabla\delta\boldsymbol{u})_b \\ &= \boldsymbol{n}_b \cdot \left\{\boldsymbol{K}_b^{-1} \cdot [\boldsymbol{n}_b\,\delta\boldsymbol{T}_b^u - \boldsymbol{n}_b\,(\boldsymbol{n}_b \cdot (\boldsymbol{C}_b : \delta\boldsymbol{E}_b)) - \boldsymbol{K}_b \cdot (\nabla\delta\boldsymbol{u})_b]\right\} \end{aligned} \tag{33}$$

To calculate the traction increment, $\delta\boldsymbol{T}_b^u$, the relationship between Cauchy traction and second Piola-Kirchhoff is employed:

$$\int_\Gamma \boldsymbol{n} \cdot \boldsymbol{\sigma}\; d\Gamma = \int_{\Gamma_u} \boldsymbol{n}_u \cdot \boldsymbol{S}_u \cdot \boldsymbol{F}\; d\Gamma_u \tag{34}$$

Additionally, Nanson's formula, relating the deformed area to the original area, is required:

$$d\boldsymbol{\Gamma} = J\boldsymbol{F}^{-1} \cdot d\boldsymbol{\Gamma}_u \tag{35}$$

Using Equations 34 and 35, the applied traction increment is given by the following relation:

$$\delta\boldsymbol{T}_b^u = \overbrace{J|\boldsymbol{F}^{-1} \cdot \boldsymbol{n}_b|\; \boldsymbol{T}_b \cdot \boldsymbol{F}^{-1}}^{\boldsymbol{T}_{\text{current}}} - \overbrace{\boldsymbol{n}_b \cdot \boldsymbol{S}_u}^{\boldsymbol{T}_{\text{old}}} \tag{36}$$

where $\boldsymbol{T}_{\text{current}}$ is the desired total traction referred to the updated area, and $\boldsymbol{T}_{\text{old}}$ is the old total traction referred to the updated area. The inverse deformation gradient, $\boldsymbol{F}^{-1}$, rotates the prescribed Cauchy stress to the updated configuration, and the term $J|\boldsymbol{F}^{-1} \cdot \boldsymbol{n}_b|$ scales the deformed area to the updated configuration.

3.3. Solution Procedure

The final discretised form of the linear momentum equation for each control volume P can be arranged in the form of a linearised algebraic equation:

$$a_P\,\delta\boldsymbol{u}_P + \sum_F a_N\,\delta\boldsymbol{u}_P = b_P \tag{37}$$

where F is the number of control volume internal faces.

The discretised coefficients, a_P and a_N, and source term b_P are:

$$a_N = -[\boldsymbol{n}_f\cdot(\boldsymbol{n}_f\cdot\boldsymbol{K}_{u_f})]\frac{|\boldsymbol{\Delta}_f|}{|\boldsymbol{d}_f|}|\boldsymbol{\Gamma}_f| \tag{38a}$$

$$a_P = -\sum_F a_N \;+\; \left\langle \left(\frac{\rho\Omega_P}{\delta t^2}\right)^{[m]} \right\rangle \tag{38b}$$

$$\begin{aligned}
b_P \;=\; & \sum_F \left[(\boldsymbol{I}-\boldsymbol{n}_f\boldsymbol{n}_f)\cdot(\boldsymbol{n}_f\cdot\boldsymbol{K}_{u_f})\right]\,\cdot(\nabla\delta\boldsymbol{u})_f|\boldsymbol{\Gamma}_f| \\
& + \sum_F \left[\boldsymbol{n}_f\cdot(\boldsymbol{n}_f\cdot\boldsymbol{K}_{u_f})\right]\boldsymbol{k}_f\cdot(\nabla\delta\boldsymbol{u})_f|\boldsymbol{\Gamma}_f| \\
& + \sum_F \boldsymbol{Q}_\Gamma^f \;+\; \rho\,(\boldsymbol{b}+\delta\boldsymbol{b})\,\Omega_P \\
& + \left\langle \left(\frac{(\rho\Omega)^{[m]}}{\delta t^{[m]}\delta t^{[m]}} + \frac{(\rho\Omega)^{[m-1]}}{\delta t^{[m]}\delta t^{[m-1]}}\right)\delta\boldsymbol{u}_P^{[m-1]} \right\rangle \\
& - \left\langle \frac{(\rho\Omega)^{[m-1]}}{\delta t^{[m]}\delta t^{[m-1]}}\delta\boldsymbol{u}_P^{[m-2]} \right\rangle \\
& - \left\langle \frac{(\rho\Omega)^{[m-1]}}{\delta t^{[m-1]}\delta t^{[m-1]}}\boldsymbol{u}_P^{[m-1]} \right\rangle \\
& + \left\langle \left(\frac{(\rho\Omega)^{[m-1]}}{\delta t^{[m-1]}\delta t^{[m-1]}} + \frac{(\rho\Omega)^{[m-2]}}{\delta t^{[m-1]}\delta t^{[m-2]}}\right)\boldsymbol{u}_P^{[m-2]} \right\rangle \\
& - \left\langle \frac{(\rho\Omega)^{[m-2]}}{\delta t^{[m-1]}\delta t^{[m-2]}}\boldsymbol{u}_P^{[m-3]} \right\rangle
\end{aligned} \tag{38c}$$

The diffusion term and source terms must be modified appropriately to include boundary condition contributions. Temporal terms are contained in $\langle\rangle$ angle brackets, and are set to zero in steady state simulations.

The algebraic linearised equation described above is then assembled for all control volumes in the mesh forming a linear system of equations:

$$[\boldsymbol{A}]\,[\boldsymbol{\phi}] = [\boldsymbol{b}] \tag{39}$$

where $[\boldsymbol{A}]$ is a sparse $N \times N$ matrix with coefficients a_P on the diagonal (N is the total number of control volumes) and F non-zero neighbour coefficients off the diagonal of the matrix, $[\boldsymbol{\phi}]$ is the solution vector of $\delta\boldsymbol{u}$ at each cell centre and $[\boldsymbol{b}]$ is the source vector.

The linear system of equations are solved in a segregated manner, with each component of the displacement field solved for separately. Outer iterations are performed to account for the inter-equation coupling and the linearised nonlinear terms. The inner linear sparse system is iteratively solved, typically using the incomplete Cholesky pre-conditioned conjugate gradient (ICCG) method [45]. Alternatively, a geometric or algebraic multigrid method may be employed potentially providing superior convergence [46, 3]. The inner system need not be solved to a fine tolerance as coefficients and source terms are approximated from the previous increment; a reduction in the residuals of one order of magnitude is typically sufficient. The outer iterations are performed until the predefined tolerance has been achieved.

At the end of each time increment, the mesh is moved to the deformed configurations. As the calculated displacements lie at the cell centres, they are interpolated to the mesh vertices using a linear least squares procedure

[44, 18].

3.4. Implementation

A distinguishing feature of OpenFOAM is that the partial differential equation and tensor operations syntax closely resembles the equations being solved. An extract of the code from the developed `elasticOrthoNonLinULSolidFoam` solver, implementing the developed orthotropic updated Lagrangian approach, is shown in given in Appendix A, and shows remarkable similarity to the previously described mathematical model.

4. Verification Cases

The developed large strain orthotropic linear elastic solver is verified by examining two separate test cases and comparing the numerical predictions to the available analytical solutions. The first test case consists of a circular hole in an orthotropic plate under tension. The second test case consists of a rotating orthotropic plate with a pressurised circular hole. Finally, in order to illustrate the capabilities of the current methodology a 3-D composite bracket with variable material principal directions is numerically examined.

Hole in an Orthotropic Plate Under Tension

The geometry, shown in Figure 2(a), consists of a square plate with a circular hole with a plate width to hole radius ratio of 200:1. The mesh of 40,000 hexahedra has been generated using the OpenFOAM utility `blockMesh`. As the case is symmetric, only one quarter of the geometry is simulated and symmetry boundary conditions are employed. The mesh is graded towards the hole, as shown in the mesh detail in Figure 2(b), in order to capture the high stress gradients without excessive mesh size. A traction of 1 MPa is applied to the right boundary of the plate in the positive x direction, and the top boundary is traction-free. Plane stress conditions are assumed.

The employed material properties are shown in Table 1, where E_i is the Young's modulus in the i direction, ν is the Poisson's ratio and G is the shear modulus. The employed mechanical properties are given with respect to the local material directions. The initial material directions in the undeformed configuration refer to the global Cartesian axes. The models have been solved using 1 CPU core (Intel Quad Core i7 2.2 GHz) where the approximate execution times varied from 90 to 170 s. The equations have been solved to an outer tolerance of 10^{-7}.

Assuming an infinite plate, the hoop stress, $\boldsymbol{\sigma}_{\theta\theta}$, around the circumference of the hole has been derived analytically by Lekhnitskii [40], and is given as:

$$\boldsymbol{\sigma}_{\theta\theta} = \boldsymbol{T} \frac{-k\cos^2\theta + (1+n)\sin^2\theta}{\sin^4\theta + (n^2 - 2k)\sin^2\theta\cos^2\theta + k^2\cos^4\theta} \tag{40}$$

where $\boldsymbol{T}$ is the applied distant load in the positive x direction, θ is the angle around the circumference of the hole with 0° on the positive x axis. Parameters k and n are given respectively by:

$$k = \sqrt{\frac{E_x}{E_y}}\,, \tag{41}$$

and

$$n = \sqrt{2k + \frac{E_x}{G_{xy}} - 2\nu_{xy}}\,. \tag{42}$$

The numerical hoop stress around the circumference of the hole is compared with the analytical solution in Figure 3. It can be seen that the numerical predictions agree closely with the analytical solution for all the examined property variations.

In order to demonstrate the applicability of the current methodology to truly unstructured meshes, the test case has also been simulated using unstructured triangular and polygonal meshes using 1 CPU core (Intel Quad Core i7 2.2 GHz) to an outer tolerance of 10^{-7}. The triangular mesh, with a detail near the hole shown in Figure 4(a), has been created using ANSYS ICEM CFD [47] and OpenFOAM utility `extrudeMesh`. The mesh is graded toward the hole and contains 98,739 cells. The approximate execution times have been from 70 to 80 s. The stress results for the triangular mesh are shown in Figure 4(b) and are shown to agree closely with the analytical solutions.

An unstructured polygonal mesh, with a detail near the hole shown in Figure 5(a), has been created by converting the triangular mesh to the Delaunay dual mesh using OpenFOAM utility `polyDualMesh`. The mesh contains 50,247 cells with approximate execution times of 30 to 40 s. The stress results for the polygonal mesh are shown in Figure 5(b) and are shown to agree closely with the analytical solutions.

In all previous test cases, the explicit divergence of stress field has been calculated using the full gradient larger computational molecule (see line 21 in Listing 1). Initially, however, as discussed in the solution implementation section, this term has been calculated using the Laplacian operator which employs a compact computational module (line 20 in Listing 1), but it has been found that the solution convergence may be poor. For the current test case, execution time is approximately 450 s and requires 2,200 outer iterations, compared with 50 s and 30 outer iterations when employing the full gradient larger computational molecule.

Rotating Orthotropic Plate with a Pressurised Hole

To examine that the developed updated Lagrangian procedure correctly rotates the constitutive stiffness tensor and the stress and strain tensors, a rotating circular plate with a pressurised hole is considered. As the plate is rotated, the location of the maximum hoop stress rotates with the corresponding rotating principal material directions. The test case geometry, shown in Figure 6(a), consists of a circular plate containing a circular hole with the ratio of outer radius to inner radius of 100:1. The mesh, shown in Figure 6(b), contains 160,000 hexahedral cells and has been generated using OpenFOAM meshing utility `blockMesh`. The mesh is graded towards the hole to reduce the total number of cells required. Plane stress conditions are assumed.

The hole is subjected to a pressure of 1 MPa and the outer plate surface is rotated through 180° in increments of 1°. The displacement increment for boundary face f is:

$$\delta \boldsymbol{u}_f = \begin{pmatrix} \cos\theta & -\sin\theta & 0 \\ \sin\theta & \cos\theta & 0 \\ 0 & 0 & 1 \end{pmatrix} \cdot \boldsymbol{C}_f \, - \, \boldsymbol{C}_f \qquad (43)$$

where θ is the increment of rotation, and $\boldsymbol{C}_f$ is the positional vector of the boundary face centre.

The employed mechanical properties with respect to the local material directions are given in Table 2. The initial material directions at time 0 correspond to the global Cartesian axes *i.e.* $1_0 = x$ and $2_0 = y$. These local material directions transform with the rotation of the plate. The model has been solved in parallel on a distributed memory computer using 32 CPU cores (Intel Xeon E5430 2.66 GHz) in an approximate clock time of 43 min. The equations have been solved to an outer tolerance of 10^{-10}. It has been found that a relatively tight outer tolerance is required when there are large rotations.

Assuming an infinite plate, the analytical solution for the hoop stress, $\boldsymbol{\sigma}_{\theta\theta}$, around the circumference of the pressurised hole has been derived by Lekhnitskii [40]:

$$\boldsymbol{\sigma}_{\theta\theta} = \boldsymbol{P}\,\frac{n - k + n(k-1)\cos^2\theta + [(k+1)^2 - n^2]\sin^2\theta\cos^2\theta}{\sin^4\theta + (n^2 - 2k)\sin^2\theta\cos^2\theta + k^2\cos^4\theta} \tag{44}$$

where $\boldsymbol{P}$ is the pressure applied to the hole, and k and n are defined previsouly.

The hoop stress around the circumference of the hole is compared with the analytical prediction for a plate rotation of 0°, 45°, 90°, 135° and 180° in Figure 7. As can be seen, the numerical predictions agree closely with the analytical predictions. At 0° rotation the largest numerical hoop stresses occur at 90.00° and 270.00° and the smallest hoop stresses at 51.09° and 128.91°, agreeing closely with analytical predictions of 90°, 70°, 51° and 129° respectively.

Figure 8 illustrates the cylindrical stress distribution in the vicinity of the hole for 0° rotation. The cylindrical stresses have been calculated in a post-processing step by transforming the Cartesian stresses. The hoop stress $\boldsymbol{\sigma}_{\theta\theta}$ can be seen to form four distinct maxima around the hole circumference. It can also be seen that the hoop stress quickly becomes independent of angle θ as the radius increases. All the stress distributions display four axes of symmetry as expected, where the shear stress $\boldsymbol{\sigma}_{r\theta}$ displays an alternating periodic distribution away from the hole surface.

The current case is also used to investigate the effects of model modification, as presented in Equation 12, to ensure equilibrium of the total forces. As highlighted in Figure 9, both the unmodified model (Equation 11) and the modified model (Equation 12) agree closely with the analytical predictions for 0° rotation. However, as can be seen for 45° rotation, significant errors accumulate in the unmodified model with increasing number of time increments. It has been found than a tighter solution tolerance can reduce the build up of errors at the expense of extra computational cost. However, the modification to the mathematical model presented in Equation 12 has been found to successfully eliminate the build up of these errors without the need for a prohibitively tight solution tolerance.

3-D Composite Component

To illustrate the applicability of the current methodology to complex geometry, a uni-directional composite bracket is numerically examined. The composite bracket geometry, shown in Figure 10(a), is meshed with 193,580 polyhedral cells. A tetrahedral Delaunay mesh has been created in ANSYS ICEM CFD and converted to the Delaunay dual mesh using OpenFOAM utility `polyDualMesh` (see mesh detail in Figure 10(b)). The Young's modulus in the composite fibre direction, given in Figure 10(a), is 50 GPa, while the Young's moduli in the transverse directions are 10 GPa. The Poisson's ratios ν_{12}, ν_{13} and ν_{23} are all set to 0.3, where direction 1 is the fibre direction, direction 3 is the positive z axis and direction 2 is orthogonal to direction 1 and 3. The shear moduli are 10 GPa. The composite bracket is fixed at the bottom left boundary and a traction of 1 MPa is applied to the top right boundary in the positive x direction. The predicted von Mises stress distribution for the composite bracket is shown in Figure 11. The maximum von Mises stress of 47 MPa is predicted to occur in the centre of the upper component surface near the bend.

To examine the parallel efficiency of the current methodology, parallel speed-up tests are performed. The 3D composite bracket has been solved on a distributed memory computer using 1, 4, 8, 16, 32, 64 and 128 CPU cores (Intel Xeon E5430 2.66 GHz) to an outer tolerance of 10^{-6}. The parallel speed-up, shown in Figure 12, is calculated as $\text{Time}_1/\text{Time}_N$, where Time_1 is the time taken on one processor and Time_N is the time taken on N processors. OpenFOAM employs a domain decomposition approach for parallel simulations where the entire geometrical domain is split across the number of available processors [4]. Here, the `scotch` decomposition method [48] is employed and the linear systems are solved using the ICCG method [45]. The execution time on 1 CPU core was 2 h 30 min. From Figure 12, it can be seen that the current methodology shows super linear parallel speed-up up to 64 cores; this may be attributed to cache effects [49]. The drop off in efficiency for 128 cores may be attributed to inter-processor communication time becoming significant with respect to the equation solution time for each relatively small processor domain ($<$ 1,600 cells per processor).

5. Conclusions

This paper is the first to develop and verify a finite volume methodology for orthotropic bodies which undergo large strains and rotations. The established procedure allows the known material properties to be specified in any natural local reference frame, and the local constitutive tensor field is then rotated to form a global constitutive tensor field which refers to the global Cartesian axes. The procedure has been verified by comparison with analytical solutions of the presented test cases, showing the applicability to structured and unstructured meshes.

The chosen test cases highlight the appropriateness of the developed methodology to examine the mechanics of orthotropic bodies undergoing large strains and large rotations. Additionally, the potential of the developed methodology has been demonstrated through examination of a realistic 3-D composite component, where impressive parallel efficiency has been shown.

Appendix A.

In order to construct the momentum equation in OpenFOAM code, the mathematical model in integral form (Equation 15) is rewritten in differential form:

$$\begin{aligned}\frac{\partial^2}{\partial t^2}\rho\,\delta\boldsymbol{u}+\frac{\partial^2}{\partial t^2}\rho\,\boldsymbol{u} \quad = \quad & \boldsymbol{K}\nabla^2\delta\boldsymbol{u} \\ & +\nabla\cdot(\boldsymbol{C}_u:\delta\boldsymbol{E}_u)\;-\;\nabla\cdot(\boldsymbol{K}\cdot\nabla\delta\boldsymbol{u}) \\ & +\nabla\cdot[(\boldsymbol{S}_u+\delta\boldsymbol{S}_u)\cdot\nabla\delta\boldsymbol{u}] \\ & +\nabla\cdot\boldsymbol{S}_u \\ & +\rho\,(\boldsymbol{b}+\delta\boldsymbol{b}) \qquad (\text{A.1})\end{aligned}$$

An extract of the code from the developed `elasticOrthoNonLinULSolidFoam` application is shown in Listing 1, and there is a remarkable similarity to the mathematical model written in differential form (Equation A.1). The `fvm::` operator indicates an implicit term, operator `fvc::` indicates an explicit term, operator `&` indicates a dot product, and operator `&&` indicates a double dot product. Comments given describe the different steps taken. A custom fourth order tensor class has been implemented and the required operators (*e.g.* double dot product) have been defined.

Listing 1: `elasticOrthoNonLinULSolidFoam` OpenFOAM Solver Code Excerpt

```
// Create material property fields
volDiagTensorField K = rheology.K();
volSymmTensor4thOrderField C = rheology.C();

// The time loop
for (runTime++; !runTime.end(); runTime++)
{
        int iCorr = 0;

        do
        {
        // Construct momentum equation
          fvVectorMatrix DUEqn
            (
             fvm::d2dt2(rho, DU)
             + fvc::d2dt2(rho, U.oldTime())
             ==
             fvm::laplacian(K, DU)
             + fvc::div(C && DEpsilon)
             // - fvc::laplacian(K, U)
             - fvc::div(K & gradDU)
             + fvc::div((sigma + DSigma) & gradDU)
             + fvc::div(sigma)
             + rho*(B+DB)
             );

        // Solve momentum equation
        solverPerf = DUEqn.solve();

        // Recalculate displacement gradient
        gradDU = fvc::grad(DU);

        // Recalculate increment of Green strain
        DEpsilon = symm(gradDU) + 0.5*symm(gradDU & gradDU.T());

        // Recalculate increment of 2nd Piola-Kirchhoff stress
        DSigma = C && DEpsilon;
    }
    while //- iterate until the explicit terms become implicit
    (
        solverPerf.initialResidual() > convergenceTolerance
```

```
42          &&
43          ++iCorr < nCorr
44      )
45      // Move mesh
46  #   include "moveMesh.H"
47
48      // Rotate fields
49  #   include "rotateFields.H
50
51      // Write fields for post-processing
52  #   include "writeFields.H"
53  }
```

Initially the *explicit* portion of the the diffusion (line 20 in Listing 1) has been calculated numerically by employing the Laplacian operator compact computational molecule. However, as is shown later in the test case section, it has been found that this form suffered from poor convergence. In addition, Demirdžić et al. [37] noted the formation of numerical oscillation twice the frequency of the mesh spacing and attributed them to the inability of the compact molecule Laplacian operator discretisation to sense the oscillations. Consequently, Demirdžić et al. [37] added a higher order term which prevents the formation of high frequency oscillations and reduced to zero otherwise. In the current study, the term is calculated by employing the full gradient across the face (line 21 in Listing 1).

References

[1] I. Demirdžić, D. Martinović, and A. Ivanković. Numerical simulation of thermal deformation in welded workpiece (in croatian). *Zavarivanje*, 31: 209–219, 1988.

[2] I. Demirdžić and S. Muzaferija. Numerical method for coupled fluid flow, heat transfer and stress analysis using unstructured moving meshes with cells of arbitrary topology. *Computer Methods in Applied Mechanics and Engineering*, 125(1-4):235–255, 1995.

[3] I. Demirdžić, S. Muzaferija and M. Perić. Benchmark solutions of some structural analysis problems using the finite-volume method and multgrid acceleration. *International Journal for Numerical Methods in Engineering*, 40:1893–1908, 1997.

[4] H. G. Weller, G. Tabor, H. Jasak, and C. Fureby. A tensorial approach to computational continuum mechanics using object orientated techniques. *Computers in Physics*, 12(6):620–631, 1998.

[5] H. Jasak and H. G. Weller. Application of the finite volume method and unstructured meshes to linear elasticity. *International Journal for Numerical Methods in Engineering*, pages 267–287, 2000.

[6] Y. D. Fryer, C. Bailey, M. Cross, and C. H. Lai. A control volume procedure for solving elastic stress-strain equations on an unstructured mesh. *Applied mathematical modelling*, 15(11-12):639–645, 1991.

[7] M. A. Wheel. A geometrically versatile finite volume formulation for plane elastostatic stress analysis. *The Journal of Strain Analysis for Engineering Design*, 31(2):111–116, 1996.

[8] M. A. Wheel. A finite volume method for analysing the bending deformation of thick and thin plates. *Computer Methods in Applied Mechanics and Engineering*, 147(1-2):199–208, 1997.

[9] I. Demirdžić and D. Martinović. Finite volume method for thermo-elasto-plastic stress analysis. *Computer methods in applied mechanics and engineering*, 109:331–349, 1993.

[10] I. Demirdžić, E. Džafarović, and A. I. Ivanković. Finite-volume approach to thermoviscoelasticity. *Numerical Heat Transfer, Part B: Fundamentals*, 47(3):213–237, 2005.

[11] I. Bijelonja, I. Demirdžić, and S. Muzaferija. A finite volume method for large strain analysis of incompressible hyperelastic materials. *International Journal for Numerical Methods in Engineering*, 64(12):1594–1609, 2005.

[12] I. Bijelonja, I. Demirdžić, and S. Muzaferija. A finite volume method for incompressible linear elasticity. *Computer Methods in Applied Mechanics and Engineering*, 195(44-47):6378–6390, 2006.

[13] I. Bijelonja. A numerical method for almost incompressible body problem. *Annals of DAAAM & Proceedings*, 22(1):321–323, 2011.

[14] P. Cardiff, A. Karač, and A. Ivanković. Development of a finite volume contact solver based on the penalty method. *Computational Material Science*, 64:283 – 284, 2012.

[15] V. Tropsa, I. Georgiou, A. Ivankovic, A. J. Kinloch, and J. G. Williams. OpenFOAM in non-linear stress analysis: Modelling of adhesive joints. In *1st OpenFOAM Workshop*, Zagreb, Croatia, 2006.

[16] H. Jasak and H. Weller. Finite volume methodology for contact problems of linear elastic solids. In *Proceedings of 3rd International Conference*

of Croatian Society of Mechanics, pages 253–260, Cavtat/Dubrovnik, Crotatia, 2000.

[17] A. Rager, J. G. Williams, and A. Ivanković. Numerical analysis of the three point bend impact test for polymers. *International Journal of Fracture*, 135(1-4):199–215, 2005.

[18] P. Cardiff. *Development of the Finite Volume Method for Hip Joint Stress Analysis*. PhD thesis, University College Dublin, 2012.

[19] A. Ivanković, I. Demirdžić, J. G. Williams, and P. S. Leevers. Application of the finite volume method to the analysis of dynamic fracture problems. *International journal of fracture*, 66(4):357–371, 1994.

[20] A. Ivanković, A. Muzaferija, and I. Demirdžić. Finite volume method and multigrid acceleration in modelling of rapid crack propagation in full-scale pipe test. *Computational mechanics*, 20(1-2):46–52, 1997.

[21] A. Ivanković and G.P. Venizelos. Rapid crack propagation in plastic pipe: predicting full-scale critical pressure from s4 test results. *Engineering Fracture Mechanics*, 59(5):607 – 622, 1998.

[22] K. Maneeratana. *Development of the finite volume method for non-linear structural applications*. PhD thesis, Imperial College London, 2000.

[23] L. Djapic Oosterkamp, A. Ivanković, and G. Venizelos. High strain rate properties of selected aluminium alloys. *Materials Science and Engineering: A*, 278(1-2):225 – 235, 2000.

[24] C.J. Greenshields, G.P. Venizelos, and A. Ivanković. A fluid-structure model for fast brittle fracture in plastic pipes. *Journal of Fluids and Structures*, 14(2):221 – 234, 2000.

[25] I. Georgiou, A. Ivanković, A.J. Kinloch, and V. Tropsa. Rate dependent fracture behaviour of adhesively bonded joints. In A. Pavan B.R.K. Blackman and J.G. Williams, editors, *Fracture of Polymers, Composites and Adhesives II*, volume 32 of *European Structural Integrity Society*, pages 317 – 328. Elsevier, 2003.

[26] I. Georgiou, H. Hadavinia, A. Ivanković, A.J. Kinloch, V. Tropsa, and J.G. Williams. Cohesive zone models and the plastically-deforming peel test. *The Journal of Adhesion*, 79:239–265, 2003.

[27] A. Karač and A. Ivanković. Investigating the behaviour of fluid-filled polyethylene containers under base drop impact: A combined experimental/numerical approach. *International Journal of Impact Engineering*, 36(4):621–631, 2009.

[28] D. Carolan, M. Petrović, A. Ivanković, and N. Murphy. Fracture properties of PCBN as a function of loading rate and temperature. *Key Engineering Materials*, 452-453:457–600, 2011.

[29] A. Karač, B.R.K. Blackman, V. Cooper, A.J. Kinloch, S. Rodriguez Sanchez, W.S. Teo, and Ivanković. Modelling the fracture behaviour of adhesively-bonded joints as a function of test rate. *Engineering Fracture Mechanics*, 78:973–989, 2011.

[30] M. Petrović, D. Carolan, A. Ivanković, and N. Murphy. Role of rate and temperature on fracture and mechanical properties of PCD. *Key Engineering Materials*, 452-453:153–156, 2011.

[31] J. Mohan, A. Karač, N. Murphy, and A. Ivanković. An experimental and numerical investigation of the mixed-mode fracture toughness and lap shear strength of aerospace grade composite joints. *Key Engineering Materials*, 488-489:549–552, 2012.

[32] D. McAuliffe, A. Karač, N. Murphy, and A. Ivanković. Transferability of adhesive fracture toughness measurements between peel and TDCB test methods for a nano-toughened epoxy. In *34th Annual Meeting of the Adhesion Society*, 2011.

[33] V. Kanyanta, A. Ivanković, and A. Karač. Validation of a fluid-structure interaction numerical model for predicting flow transients in arteries. *Journal of Biomechanics*, 42(11):1705–1712, 2009.

[34] A. Kelly and M. J. O'Rourke. Two system, single analysis, fluid-structure interaction modelling of the abdominal aortic aneurysms. *Proceedings of the Institution of Mechanical Engineers Part H - Journal of Engineering in Medicine*, 224(H8):955–970, 2010.

[35] A. Kelly and M. J. O'Rourke. Fluid, solid and fluid-structure interaction simulations on patient-based abdominal aortic aneurysm models. *Proceedings of the Institution of Mechanical Engineers Part H - Journal of Engineering in Medicine*, 226(4):288–304, 2012.

[36] J. Fainberg and H. J. Leister. Finite volume multigrid solver for thermoelastic analysis in anisotropic materials. *Comput. Methods. Appl. Mech. Engrg.*, 137:167–174, 1996.

[37] I. Demirdžić, I. Horman, and D. Martinović. Finite volume analysis of stress and deformation in hygro-thermo-elastic orthotropic body. *Computer Methods in Applied Mechanics and Engineering*, 190:1221–1232, 2000.

[38] The OpenFOAM Extend Project. `http://www.extend-project.de`, 2012.

[39] The OpenFOAM Foundation. `http://www.openfoam.org`, 2012.

[40] S. Lekhnitskii. *Theory of Elasticity of an Aniostropic Body.* Mir Publishers, 1981.

[41] K. J. Bathe. *Finite element procedures.* Prentice-Hall, New Jersey, 1996.

[42] K. J. Bathe. Res.2-002 finite element procedures for solids and structures, spring. MIT OpenCourseWare, 2010.

[43] Ž. Tuković and H. Jasak. Updated lagrangian finite volume solver for large deformation dynamic response of elastic body. *Transactions of FAMENA*, 1(31):1–16, 2007.

[44] P. Cardiff, A. Karač, Ž. Tuković, and A. Ivanković. Development of a finite volume based structural solver for large rotation of non-orthogonal meshes. In *7th OpenFOAM Workshop*, Darmstadt, Germany, 2012.

[45] D. A. H. Jacobs. Preconditioned conjugate gradient methods for solving systems of algebraic equations. *Central Electricity Research Laboratories Report*, RD/L/N193/80, 1980.

[46] S. Muzaferija. *Adaptive Finite Volume Method Flow Prediction Using Unstructured Meshes and Multigrid Approach*. British Thesis Service. University of London, 1994.

[47] ANSYS Inc. ANSYS ICEM CFD 13.0 user manual. `http://www.ansys.com/Products/Other+Products/ANSYS+ICEM+CFD`, 2011.

[48] C. Chevalier and F. Pellegrini. PT-SCOTCH: a tool for efficient parallel graph ordering. *Parallel Computing*, 34:318–331, 2008.

[49] T. N. Venkatesh, V. R. Sarasamma, S. Rajalakshmy, K. C. Sahu, and R. Govindarajan. Super-linear speed-up of a parallel multigrid navier-stokes solver on flosolver. *Current Science*, 88:589–593, 2005.

[50] H. Jasak. Dynamic mesh handling in OpenFOAM. In *American Institute of Aeronautics and Astronautics*, pages 1–10, 2007.

List of Figures

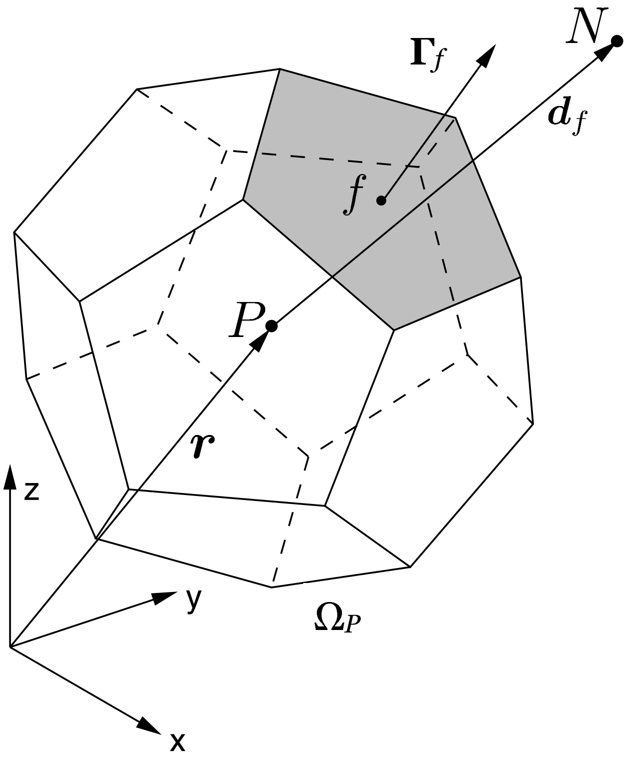

Figure 1: General Polyhedral Control Volume (Adapted from [2, 50])

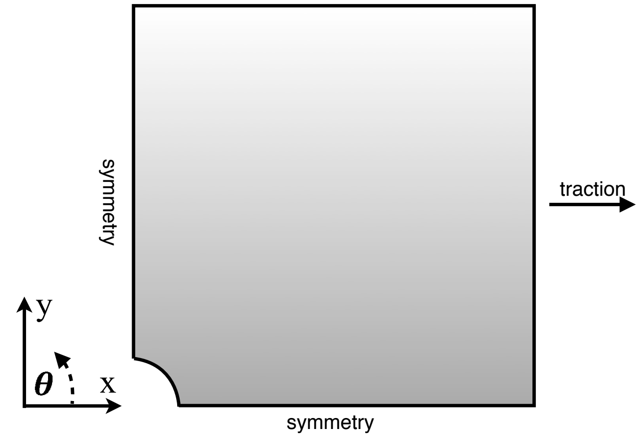

(a) Geometry & Loading

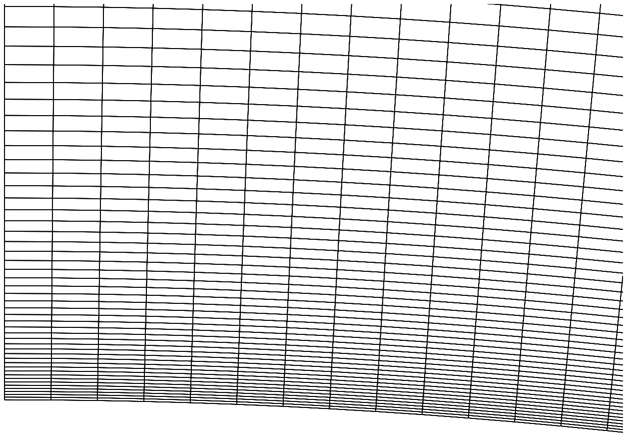

(b) Close-up View of Mesh Near the Hole

Figure 2: Orthotropic *Hole-in-a-Plate* Test Case

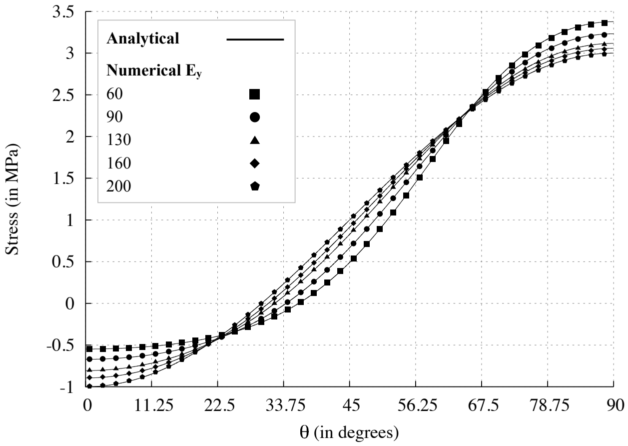

Figure 3: Hoop Stress Around Circumference of the Hole - Orthotropic *Hole-in-a-Plate* Test Case with Hexagonal Mesh

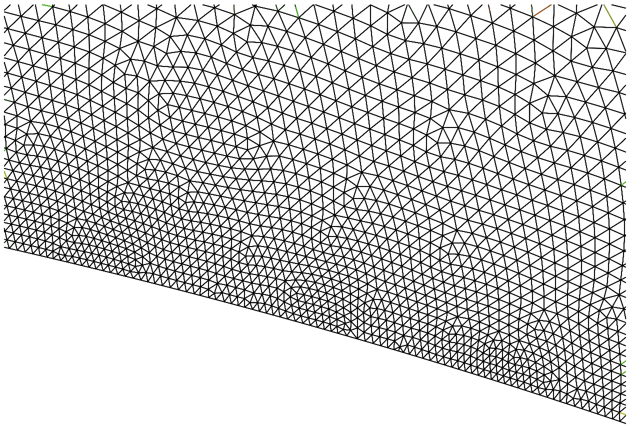

(a) Mesh Near the Hole

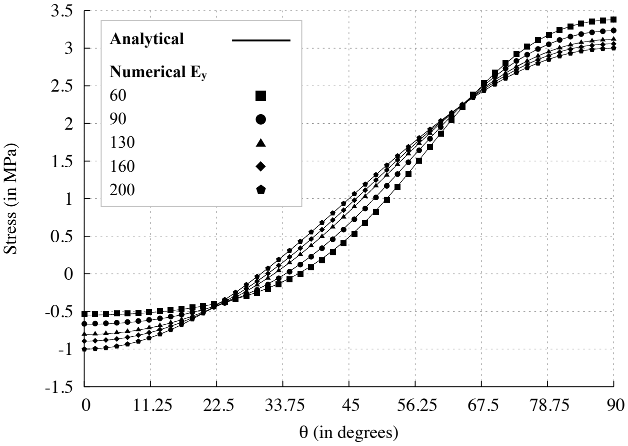

(b) Hoop Stress Around Hole

Figure 4: Orthotropic *Hole-in-a-Plate* Test Case with Triangular Mesh

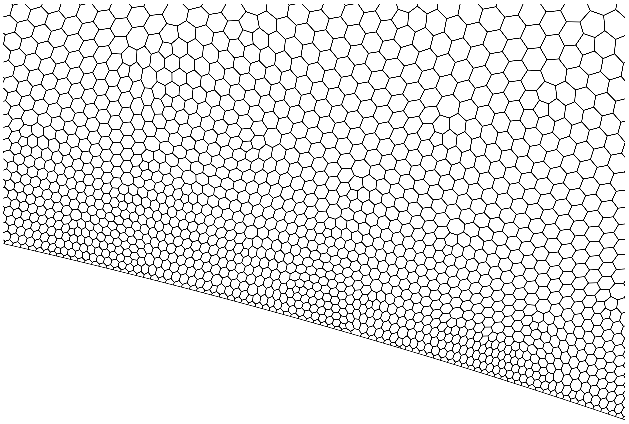

(a) Mesh Near the Hole

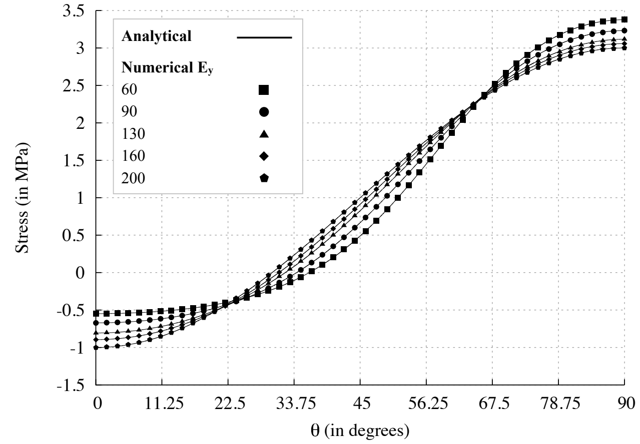

(b) Hoop Stress Around Hole

Figure 5: Orthotropic *Hole-in-a-Plate* Test Case with Polygonal Mesh

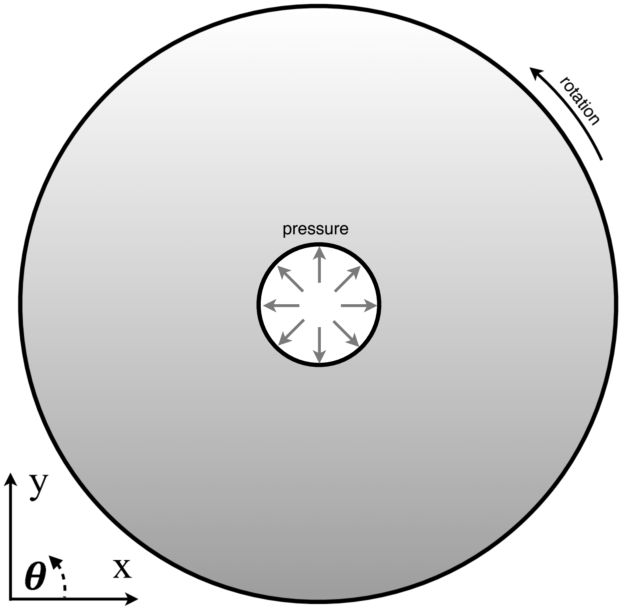

(a) Geometry

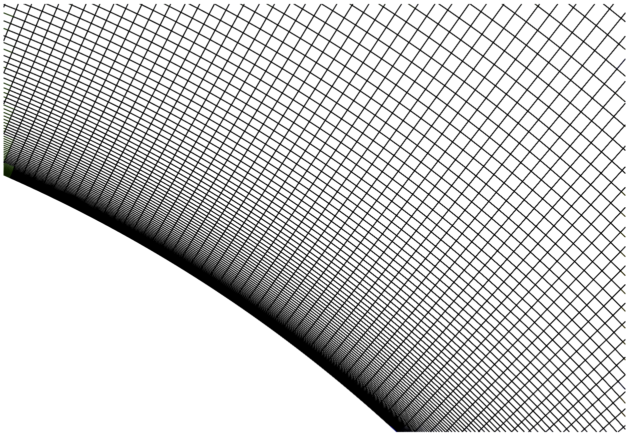

(b) Mesh Near the Hole

Figure 6: Rotating Orthotropic Plate Geometry and Mesh

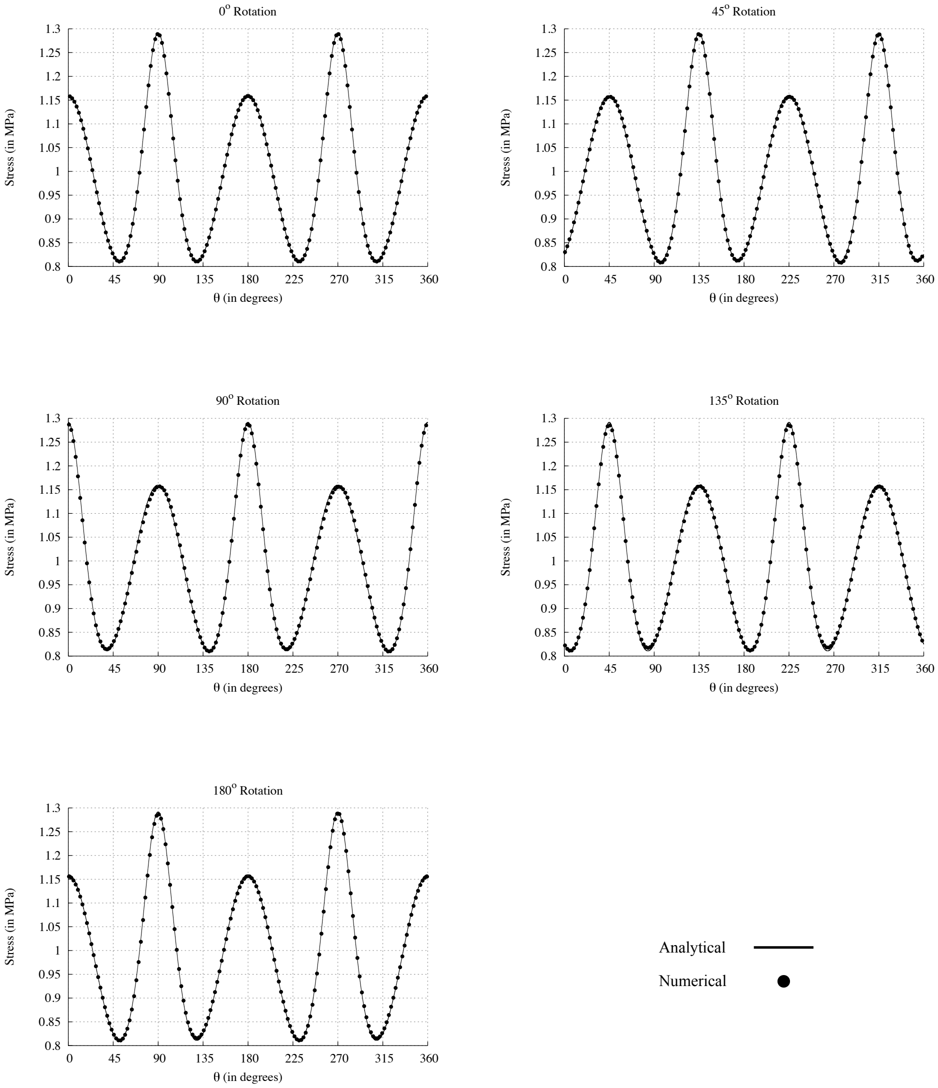

Figure 7: Rotating Orthotropic Plate with Pressurised Hole - Hoop Stress for Different Rotation Angles

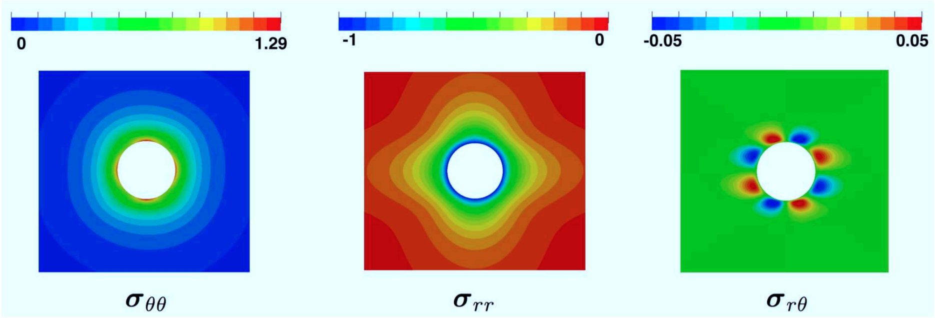

Figure 8: Rotating Orthotropic Plate with Pressurised Hole - Stress Distribution at 0° Rotation (in MPa)

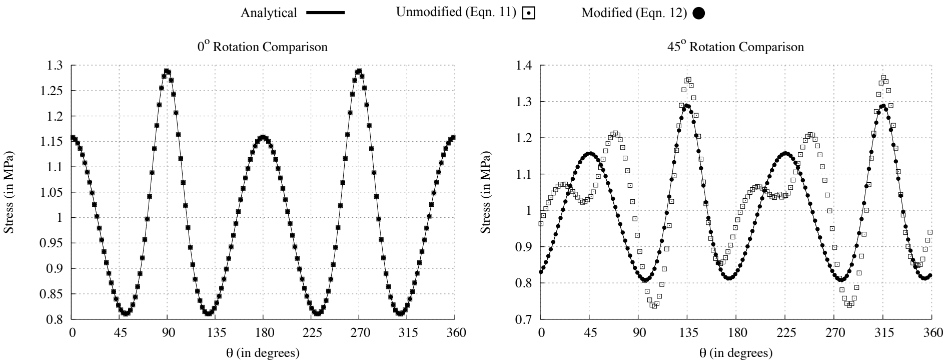

Figure 9: Unmodified Mathematical Model Showing Error Accumulation

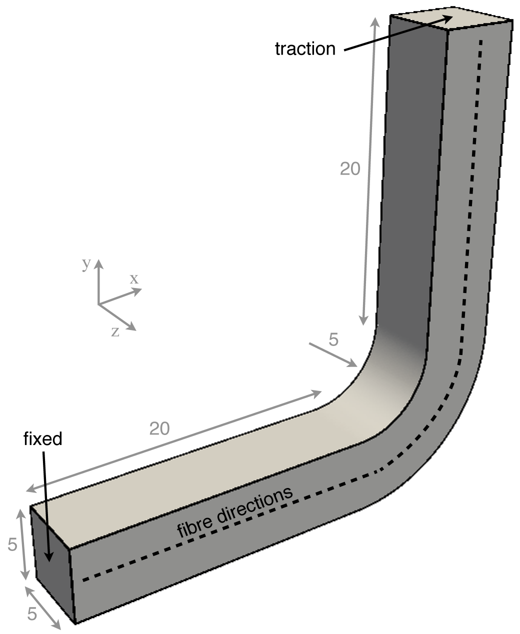

(a) Geometry (in mm)

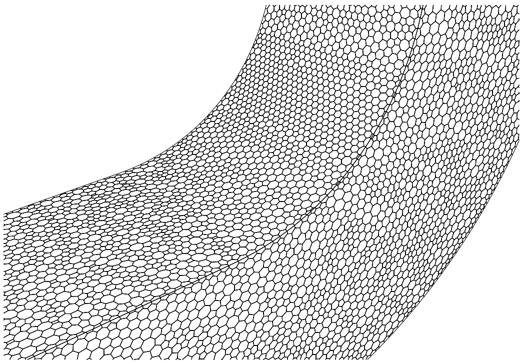

(b) Polyhedral Mesh

Figure 10: Composite Component

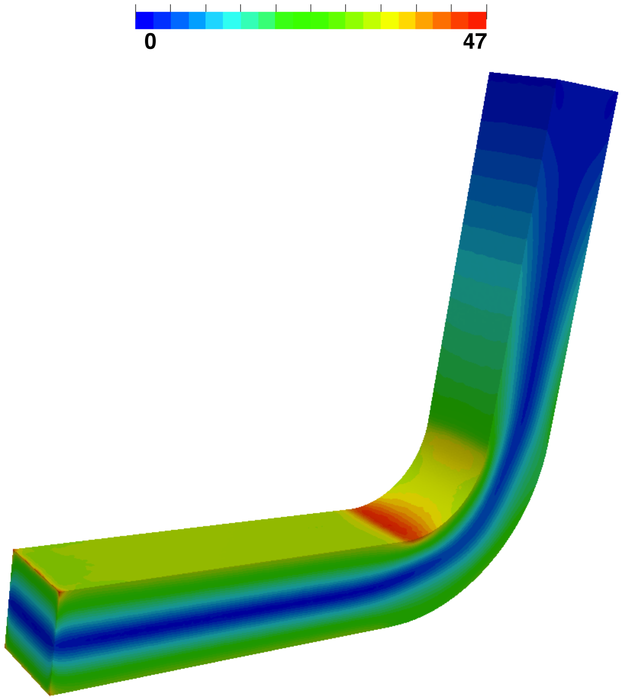

Figure 11: Composite Component von Mises Stress Distribution (in MPa)

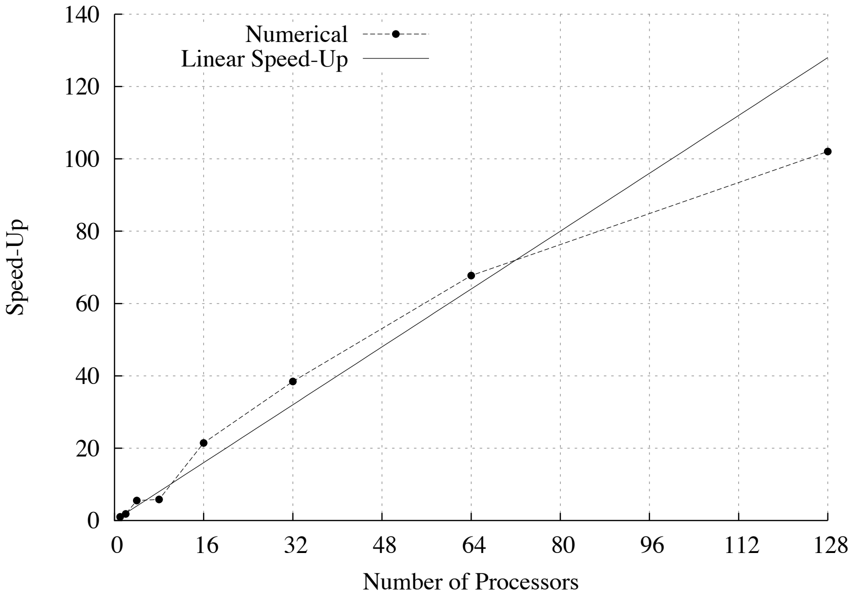

Figure 12: Composite Component Parallel Speed-Up

List of Tables

Property	Value
E_x	200 GPa
E_y	varied from 60 - 200 GPa
ν_{xy}	0.3
G_{xy}	76.92 GPa

Table 1: Plate Orthotropic Material Properties

Property	Value
E_1	200 GPa
E_2	60 GPa
ν_{12}	0.3
G_{12}	76.92 GPa

Table 2: Rotating Orthotropic Plate Material Properties